Enhanced 4x4 MIMO RoF architecture for 5G mmWave indoor applications at 60 GHz unlicensed band

Hachim Azzahhafi, Moussa El Yahyaoui, Ali El Moussati, Ghais El Zein, Ana Garcia Armada

Enhanced 4x4 MIMO RoF Architecture for 5G mmWave Indoor Applications at 60 GHz Unlicensed Band

Authors

Hachim Azzahhafi [a], Moussa El Yahyaoui [a], Ali El Moussati [a], Ghaïs El Zein [b], Ana Garcia Armada [c]

[a] Department of Electronics, Informatics and Telecommunications, ENSAO, Oujda, Morocco

[b] Univ Rennes, INSA Rennes, CNRS, IETR, UMR 6164, F 35000, Rennes, France

[c] Department of Signal Theory and Communications, Universidad Carlos III de Madrid, Spain

Keywords

5G NR, RoF, MIMO, mmWave, 60 GHz, TSV channel.

Abstract

4x4 Multiple Input Multiple Output (MIMO) optical architecture based on Radio over Fiber (RoF) is proposed for 5G millimeter Wave (mmWave) indoor applications in the unlicensed 60 GHz band. First-order and second-order sidebands, generated by Dual-Drive Mach–Zehnder Modulator (DD-MZM), are exploited as optical subcarriers in order to reduce the number of Local Oscillators (LOs) implemented. Four MIMO-OFDM signals are multiplexed using Dual-Parallel Mach–Zehnder Modulator (DP-MZM) configured to perform Optical Carrier Suppression (OCS) modulation. 60 GHz spacing is ensured between each data signal and its corresponding subcarrier which allows simple heterodyne detection at Radio Access Point (RAP) level. In addition, we have proposed a 4x4 MIMO extension of Triple-S-and-Valenzuela (TSV) radio channel model based on geometrical approach. We demonstrate that the proposed RoF system with adequate configuration can meet the 5G New Radio (NR) requirement in terms of Error Vector Magnitude (EVM). Moreover, Bit Error Rate (BER) performance is evaluated with and without 5G NR channel coding, for transmission over 25 km of optical fiber followed by 3 m of radio channel, by exploiting the overall allocated band at 60 GHz which allows to achieve a very high data rate up to 122.5 Gb/s.

1. Introduction

The 5th generation (5G) has changed the concepts of wireless mobile communication systems that were focused only on increasing data rate and providing services for personal use. The 5G technology is developed to respond to the huge demand for new applications and services for both personal and professional uses, such as the Internet of Things (IoT), Augmented Reality (AR), Cloud Computing and Gaming, Smart Building, Industry Automation and Mission Critical Applications [1]. To meet these diverse challenges, 5G systems are expected to support three typical use cases, namely enhanced Mobile Broadband (eMBB), massive Machine Type Communications (mMTC) and Ultra Reliable Low Latency Communications (URLLC) [1].

Key enabling radio access technologies such as millimeter Wave (mmWave) communication, Multiple Input Multiple Output (MIMO) technology, Orthogonal Frequency Division Multiplexing (OFDM) numerology and Low-Density Parity-Check (LDPC) codes have been specified by 3rd Generation Partnership Project (3GPP), the organization in charge of standardization and specification of the 5G, under the name of New Radio (NR) technologies [2,3]. The main aim to adopt frequencies in the mmWave bands (30–300 GHz), is not only to mitigate the burden on the sub-6 GHz frequency band, but also to exploit its large bandwidth which directly leads to

increase the data rate and reduce latency with higher numerologies. Moreover, the propagation loss in the mmWave, which was seen previously as a drawback, is considered now the main feature to support short-range applications in ultra-dense and indoor environments [4,5].

Currently, the licensed 28 GHz band is the adopted mmWave band for deploying 5G NR technologies. However, to ensure more capacity and flexibility in terms of technologies and applications, the 3GPP has started scaling 5G NR design to support unlicensed bands, specifically the 60 GHz band. The specification of this band, known as NR Unlicensed (NR-U), has been recently included as a part of release 17 [6]. The 60 GHz band, exploited by well-known wireless standards such as IEEE 802.15.3c [7], IEEE 802.11ad [8], and IEEE 802.11ay [9], offers four channels with high bandwidths up to 8.64 GHz [9]. Several works have dealt with the coexistence of 5G NR-U and IEEE 802.11 technologies [10–13]. The fact that the radio coverage of 60 GHz band is limited to a few meters and waves at this frequency cannot penetrate walls makes it more suitable for 5G In-Building applications. Moreover, to ensure 5G connectivity in the entire building, the radio coverage needs to be expanded. The most viable solution to reach this aim is based on using a network of Radio Access Points (RAPs) supported by Radio over Fiber (RoF) technology. By deploying this solution, a building can be covered by multiple small cells served by low-cost RAPs. These RAPs are linked, using RoF technology, to a centralized Base Station (BS) where high-complexity signal processing is performed.

RoF technology has attracted attention in recent years because of its many benefits such as the large bandwidth and low attenuation offered by the optical fiber. Moreover, the RAPs are simplified thanks to centralized processing at BS. Another advantage of RoF is the possibility to exploit the existing optical fiber networks [14]. To distribute signals between RAPs and BS, there are three different categories of RoF, namely Base Band over Fiber (BBoF), Intermediate Frequency-over-Fiber (IFoF), and Radio Frequency-over-Fiber (RFoF)[15]. The latter is the most suitable in our case since the 60 GHz signals are processed at BS and transported via an optical fiber to RAPs where the 60 GHz signals are photo-detected and directly transmitted on the air interface using antennas. By adopting this configuration, the RAPs complexity and cost are reduced. In addition, the fact that all complex treatments are carried out at the centralized BS makes this system easy to upgrade, which is a fundamental feature of 5G systems [16].

To guarantee high capacity and reliable communications, RoF systems can be endowed with MIMO technology. The straightforward solution to transport independent MIMO signals is to use as many optical links as there are MIMO channels, which leads to an increase in deployment costs. Several works have dealt with this challenge by using different multiplexing schemes to transport mmWave MIMO signals over a single optical link, including Wavelength Division Multiplexing (WDM)[17], Polarization Division Multiplexing (PDM)[18] and Optical Subcarriers Multiplexing (OSCM)[19].

In the WDM scheme, each MIMO channel requires an optical source and optical modulator. Moreover, high frequency Local Oscillators (LOs) are required to transport mmWave signals using this scheme. The complexity of this scheme increases by increasing the number of antennas in the MIMO system. In [18], a PDM scheme has been proposed to transport a 2x2 MIMO signal at 60 GHz, where a dual tone laser source is used to feed two independent Dual-Drive Mach–Zehnder Modulators (DD-MZMs). In addition, two LOs are implemented to perform frequency translation of OFDM signals. The authors in [19] used OSCM to transport 2x2 MIMO over Single Mode Fiber (SMF) by using Dual-Parallel Mach–Zehnder Modulators (DP-MZM) and two LOs. However, these architectures are limited to transport only 2x2 MIMO signals. The 4x4 MIMO version of these systems requires using two optical links or a combination with WDM scheme. These solutions increase the complexity of the system and are not cost-effective. In our previous works [20,21], we have introduced two optical schemes to transport 2x2 MIMO signals

at 60 GHz, where two MIMO-OFDM signals combined with two optical subcarriers are generated and transmitted over optical fiber. These proposed RoF systems achieve a data rate up to 70 Gb/s.

In this work, we further improve our system by proposing a new 4x4 MIMO scheme which allows to reach a higher data rate up to 122 Gb/s. This proposal uses one optical link fed by one laser source and only three LOs. Frequency-Division Multiplexing (FDM) is performed to combine four OFDM signals by using two LOs. These signals are fed to a DP-MZM biased to perform Optical Carrier Suppression (OCS) modulation which leads to generate four independent optical MIMO signals. Our architecture allows the use of simple heterodyne detection using Photodiodes (PDs) to generate 60 GHz signals to be transmitted over the radio channel. For this purpose, four optical subcarriers, corresponding to the first and the second order optical sidebands, are generated by a DD-MZM driven by the third LO. This optical modulator is configured to perform OCS modulation with the third-order sidebands suppression. The use of both the first and the second order sidebands as optical subcarriers in this work, is supported by the fact that the Signal to Noise Ratio (SNR) does not depend on the power level of the optical subcarriers in the heterodyne detection technique at receiver [22]. The frequencies delivered by the LOs are well chosen to guarantee 60 GHz between each OFDM signal/subcarrier pair. The optical subcarriers are combined with the optical OFDM-MIMO signals by using an optical coupler. This resulting optical signal is transmitted over fiber to the RAP.

Moreover, to evaluate the performance of our RoF system for indoor applications, we introduce a 4x4 MIMO extension of the Triple-S and Valenzuela (TSV) channel model based on geometrical approach. This model was first proposed as a realistic Single Input Single Output (SISO) channel to model indoor environments for the 802.15.3c standard [23]. For performance evaluation, channel coding schemes are implemented in this work, according to the 5G NR specifications for multiplexing and channel coding [24].

The rest of this paper is organized as follows: Section 2 presents the proposed 4x4 MIMO optical architecture. Section 3 introduces the 4x4 MIMO extension of the TSV channel model. In Section 4, we present the obtained results and discussions. Finally, conclusions are given in Section 5.

2. Proposed 4x4 MIMO optical architecture

The proposed 4x4 MIMO RoF architecture transmitting signals from the BS to the RAP is presented in **Error! Reference source not found.**, where four baseband complex signals, obtained by performing OFDM modulation are converted to electrical signals by using I/Q mixers. The first two obtained signals, corresponding to the transmit antennas *Tx1* and *Tx2*, are up-converted in frequency using two local oscillators LO1 and LO2 of frequencies $f_{\mathrm{LO1}} = 12$ GHz and $f_{\mathrm{LO2}} = 36$ GHz, respectively. These signals are then frequency multiplexed as shown in inset (a). The same processing is performed on the second two signals, corresponding to the transmit antennas *Tx3* and *Tx4*, the corresponding multiplexed signal is shown in inset (a'). The two resulting multiplexed signals are coupled through a 90° hybrid coupler. The phase-shifted outputs of the hybrid coupler, shown in insets (b) and (b'), drive the optical modulator based on DP-MZM. This component is described in detail in subsection 2.1.

The modulated optical MIMO signals at the output of DP-MZM, shown in inset (c), are coupled with four optical subcarriers generated using DD-MZM modulator by exploiting first-order and second-order sidebands. This modulator is driven by a signal delivered from a third local oscillator at $f_{\mathrm{LO3}} = 24$ GHz. The DD-MZM configuration is mathematically demonstrated in

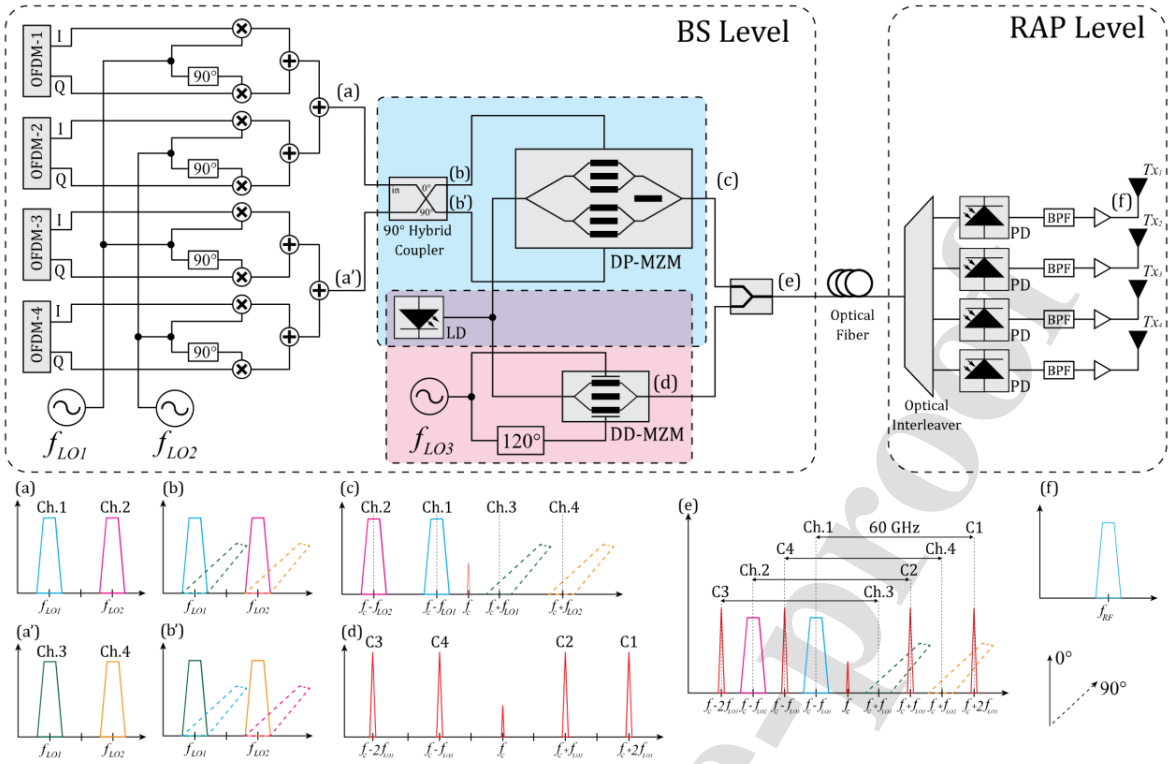

Fig. 1. The proposed optical architecture.

subsection 2.2. Subsequently, the resulting optical MIMO signal, corresponding to inset (e), is transmitted through the optical fiber to the RAP.

The received optical signal is interleaved to separate the four optical components of the 4x4 MIMO signal. Indeed, the frequencies of the local oscillators employed in this design were chosen to be multiples of 12 GHz, allowing us to separate all components using a demultiplexer with a frequency spacing of 12 GHz. The channels are then merged with their respective subcarriers to achieve 60 GHz spacing. Finally, four PDs are placed to perform heterodyne detection to generate four electrical signals at $f_{\mathrm{RF}} = 60$ GHz. These signals are then filtered, amplified, and transmitted over the MIMO wireless channel, as shown in inset (f).

2.1. Data modulation using DP-MZM

Our proposal is based on OCS for data modulation using DP-MZM. To perform this kind of modulation, a continuous optical carrier generated at f_c, by the Laser Diode (LD), is fed to the DP-MZM, which is biased by using appropriate parameters to realize OCS modulation. The DP-MZM used in this work is based on [25]. This modulator consists of three sub-MZMs which can be controlled separately to change their working points. A detailed schematic of the DP-MZM with OCS configuration is shown in Fig. 2.

The first output of the hybrid coupler, shown in inset (a) of Fig. 2 drives differentially the first sub-MZM biased at its switching voltage $V_{bias1} = V_{\pi}^{DP}$ which leads to perform double-side band (DBS) modulation and generate the first DBS signal shown in inset (b) of Fig. 2, whereas the second output, in inset (a') of Fig. 2, drives the second sub-MZM using the same configuration i.e., $V_{bias2} = V_{\pi}^{DP}$ and a second DBS signal shown in inset (b') of Fig. 2 is generated. The third sub-MZM, which acts as an optical phase shifter, is biased at $V_{bias3} = \frac{V_{\pi}^{DP}}{2}$ to have a $\frac{\pi}{2}$ phase difference between the two DSB Signals. By using this configuration, these DBS signals are

superposed in a manner to have constructive and destructive interference allowing the separation of the overlapped components and creating the signal shown in inset (d) of Fig. 2. The main parameters of the DP-MZM are shown in Table 1.

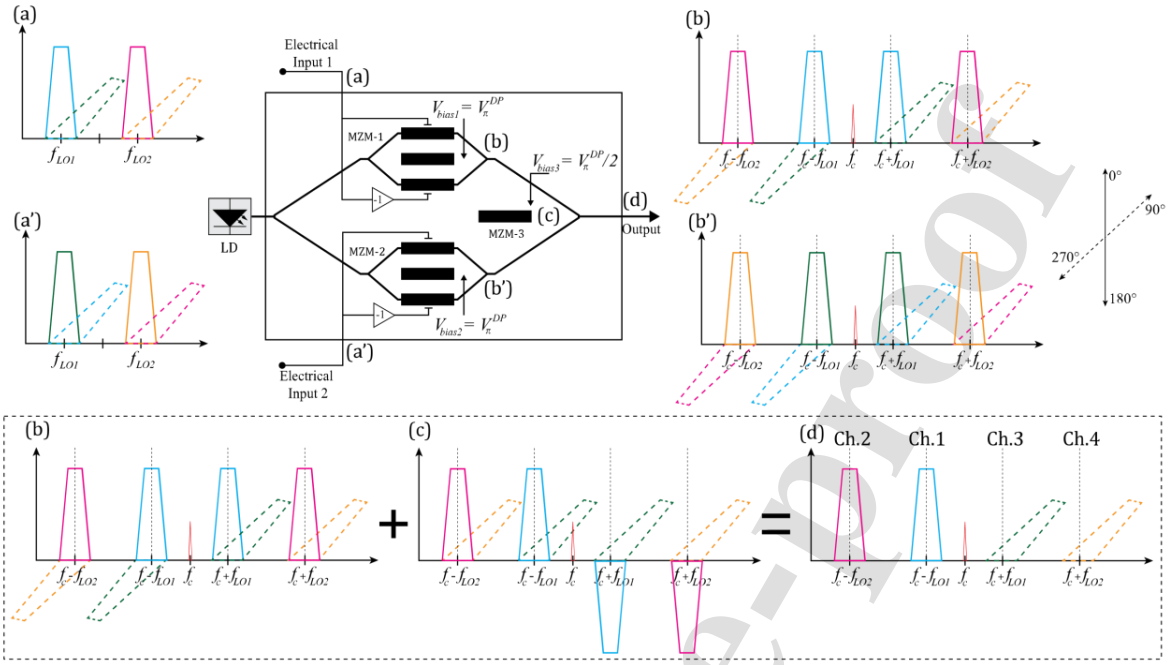

Fig. 2. Detailed schematic of the DP-MZM with OCS configuration.

Table 1. Main parameters of the DP-MZM.

Parameter	value
Extinction ratio	30 dB
Switching voltage V_π^{DP}	4 volt
Bias voltage 1	4 volt
Bias voltage 2	4 volt
Bias voltage 3	2 volt

2.2. Optical subcarriers generation

Our proposal is based on optical heterodyne detection at the RAP to generate four electrical signals to be transmitted at $f_{\mathrm{RF}} = 60$ GHz using MIMO antennas as depicted in **Error! Reference source not found.**. In addition to the optical data-signals generated by DP-MZM, the optical heterodyne technique needs to have four optical subcarriers positioned at well-chosen frequencies to be detected by the PDs. To achieve that, we have opted for an optical subcarrier generation using DD-MZM powered by the LD and driven by the electrical output of the local oscillator at $f_{LO3} = 24$ GHz. Two optical subcarriers are positioned at $f_c - f_{LO3}$ and $f_c + f_{LO3}$ which represent the first-order sidebands and the other subcarriers are positioned at $f_c - 2f_{LO3}$ and $f_c + 2f_{LO3}$ which represent the second-order sidebands. This electrical signal is expressed as

$$V_{LO3}(t) = V_m \cos(2\pi f_{LO3} t) \tag{1}$$

where V_m is the peak amplitude of the signal.

The optical field of the signal generated by the DD-MZM is expressed as follows [14]

$$E_{DD-MZM}(t) = \frac{E_{Laser}(t)\sqrt{t_{attn}}}{2}\left[e^{j\frac{\pi}{V_\pi^{DD}}V_1(t)} + e^{j\frac{\pi}{V_\pi^{DD}}V_2(t)}\right] = \sqrt{\frac{P_{Laser}\, t_{attn}}{2}}\left[e^{j\frac{\pi}{V_\pi^{DD}}V_1(t)} + e^{j\frac{\pi}{V_\pi^{DD}}V_2(t)}\right]e^{j2\pi f_c t} \quad (2)$$

where $E_{Laser}(t)$, P_{Laser}, and $f_c = \frac{\omega_c}{2\pi}$ are the optical field, the transmit power and the optical carrier frequency of the LD, respectively. t_{attn} is the insertion loss of the modulator and V_π^{DD} is the switching voltage of the DD-MZM, i.e., the voltage which results in a phase change of π radians in the signal propagating in the arm where it is applied. $V_1(t)$ and $V_2(t)$ are the driving signals applied in the first arm and in the second arm of the DD-MZM respectively, and are expressed as

$$V_1(t) = V_m \cos(2\pi f_{LO3} t) + V_{bias}^{DD} \quad (3)$$

$$V_2(t) = V_m \cos(2\pi f_{LO3} t + \theta) \quad (4)$$

where V_{bias}^{DD} is the bias voltage added to $V_{LO3}(t)$ in the first arm of the DD-MZM (the bias voltage of the second arm is fixed to 0 volt). θ is the phase of the electrical phase shifter placed at the input of the second arm as depicted in **Error! Reference source not found.**.

By inserting Eq. (3) and Eq. (4) into Eq. (2), it is obtained

$$E_{DD-MZM}(t) = \sqrt{\frac{P_{Laser}\, t_{attn}}{2}}\left[e^{j\frac{\pi}{V_\pi^{DD}}(V_m\cos(2\pi f_{LO3}t)+V_{bias}^{DD})} + e^{j\frac{\pi}{V_\pi^{DD}}V_m\cos(2\pi f_{LO3}t+\theta)}\right]e^{j2\pi f_c t} \quad (5)$$

For simplicity, Eq. (5) can be rewritten as

$$E_{DD-MZM}(t) = E_{attn}\left[e^{(jm\cos(2\pi f_{LO3}t)+j\pi\gamma)} + e^{jm\cos(2\pi f_{LO3}t+\theta)}\right]e^{j2\pi f_c t} = E_{attn}\left[e^{jm\cos(2\pi f_{LO3}t)}e^{j\pi\gamma} + e^{jm\cos(2\pi f_{LO3}t+\theta)}\right]e^{j2\pi f_c t} \quad (6)$$

where $E_{attn} = \sqrt{\frac{P_{Laser}\, t_{attn}}{2}}$, $m = \pi\frac{V_m}{V_\pi^{DD}}$ is the modulation index of the DD-MZM and $\gamma = \frac{V_{bias}^{DD}}{V_\pi^{DD}}$ is its normalized bias voltage. From Jacobi-Anger expansion [26], Eq. (6) becomes

$$E_{DD-MZM}(t) = E_{attn}\sum_{n=-\infty}^{+\infty} j^n J_n(m)\left(e^{jn(2\pi f_{LO3}t)}e^{j\pi\gamma} + e^{jn(2\pi f_{LO3}t)}e^{jn\theta}\right)e^{j2\pi f_c t} = E_{attn}\sum_{n=-\infty}^{+\infty} j^n J_n(m)\left(e^{j\pi\gamma} + e^{jn\theta}\right)e^{j2\pi(f_c+nf_{LO3})t} \quad (7)$$

where $J_n(m)$ is the n^{th} Bessel function of the first kind. By observing Eq. (7), the optical field generated from the DD-MZM consists of an optical carrier and sidebands with infinite order. However, the order of most important sidebands, in terms of power, can be adjusted by changing the amplitude of the signal emitted by LO and consequently the modulation index *m*. For our case, the sidebands of 0^{th}, 1^{st}, 2^{nd}, and 3^{rd} order are the most important, while the sidebands of order $n \geq 4$ are neglected. Then we list the optical fields of these sidebands

$$E_{-3} = E_{attn}.J_{-3}(m).\left(e^{j\pi\gamma} + e^{-j3\theta}\right).e^{j2\pi(f_c-3f_{LO3})t}.e^{j\frac{\pi}{2}}$$

$$E_{-2} = E_{attn}.J_{-2}(m).\left(e^{j\pi\gamma} + e^{-j2\theta}\right).e^{j2\pi(f_c-2f_{LO3})t}.e^{j\pi}$$

$$\begin{aligned} E_{-1} &= E_{attn}.J_{-1}(m).\left(e^{j\pi\gamma}+e^{-j\theta}\right).e^{j2\pi(f_c-f_{LO3})t}.e^{-j\frac{\pi}{2}} \\ E_0 &= E_{attn}.J_0(m).\left(e^{j\pi\gamma}+1\right).e^{j2\pi f_c t} \\ E_1 &= E_{attn}.J_1(m).\left(e^{j\pi\gamma}+e^{j\theta}\right).e^{j2\pi(f_c+f_{LO3})t}.e^{j\frac{\pi}{2}} \\ E_2 &= E_{attn}.J_2(m).\left(e^{j\pi\gamma}+e^{j2\theta}\right).e^{j2\pi(f_c+2f_{LO3})t}.e^{j\pi} \\ E_3 &= E_{attn}.J_3(m).\left(e^{j\pi\gamma}+e^{j3\theta}\right).e^{j2\pi(f_c+3f_{LO3})t}.e^{-j\frac{\pi}{2}} \end{aligned} \quad (8)$$

In order to realize the OCS modulation combined with the third-order sidebands suppression, the conditions below should be verified

$$\begin{aligned} &e^{j\pi\gamma}+1=0 \\ &e^{j\pi\gamma}+e^{-j3\theta}=0 \\ &e^{j\pi\gamma}+e^{j3\theta}=0 \\ &e^{j\pi\gamma}+e^{jn\theta}\neq 0 \text{ with } n=1;2. \end{aligned} \quad (9)$$

By solving this system of equations, we have

$$\gamma=\frac{V_{bias}^{DD-MZM}}{V_{\pi}^{DD}}=2k+1 \text{ with } k\in\mathbb{Z} \text{ and } \theta=\frac{2\pi}{3}\ (mod\ 2\pi) \quad (10)$$

Therefore, the DD-MZM must be biased at $V_{bias}^{DD}=V_{\pi}^{DD}$ and the phase shifter placed must be configured to have $\theta=120°$.

3. 4x4 MIMO extension of the TSV channel model

3.1. TSV channel model

We consider the TSV channel model, proposed by the National Institute of Information and Communication Technology (NICT) [27]. This model was used, in the framework of IEEE 802.15.3c standardization, as a realistic indoor channel model for mmWave band at 60 GHz. Indeed, the TSV model is based on statistical models validated by several experimental results and analysis for different types of environments, such as Office, Library, Kiosk and Desktop, for both Line of Sight (LoS) and non-LoS (NLoS) links.

In this work, we are interested in the LoS desktop environment. For this environment, the transmission channel behavior can be modeled by merging two well-known channel models. For LoS path components, the two-path model is dominantly observed, as for the NLoS path components, the SV model is adopted [23]. Then, the Channel Impulse Response (CIR) of the TSV model is expressed in function of the CIR of the two-path model, $h_{\text{two}}(t)$, and the CIR of the SV model $h_{\text{sv}}(t)$ as follows

$$h_{\text{tsv}}(t,\varphi)=h_{\text{two}}(t)+h_{\text{sv}}(t,\varphi) \quad (11)$$

where $h_{\text{two}}(t)$ is expressed as follows

$$h_{\text{two}}(t)=\beta\delta(t)=\left(\frac{\lambda}{4\pi D}\right)^2\left|\sqrt{G_{Tx}^{(1)}G_{Rx}^{(1)}}+\sqrt{G_{Tx}^{(2)}G_{Rx}^{(2)}}R_0\exp\left[j\frac{2\pi}{\lambda}\frac{2h_{Tx}h_{Rx}}{D}\right]\right|\delta(t) \quad (12)$$

where $\delta(.)$, β, λ, h_{Tx}, h_{Rx}, D and R_0 denote the Dirac delta function, the path gain for LOS component, the wavelength, the height of Tx antenna, that of Rx antenna, the Tx-Rx distance separation and the reflection coefficient of the desk, respectively. $G_{Tx}^{(1)}$, $G_{Tx}^{(2)}$, $G_{Rx}^{(1)}$ and $G_{Rx}^{(2)}$ are the Tx antenna gain for the direction of direct path direction (path 1), the Tx antenna gain for the

reflected path direction (path 2), the Rx antenna gain for the direct path direction, and the Rx antenna gain for the reflected path direction, respectively.

Then, $h_{\mathrm{sv}}(t)$ is expressed as a function of time-invariant random parameters as follows

$$h_{\mathrm{sv}}(t,\varphi)=\sum_{l=1}^{L}\sum_{m=1}^{M_l}\alpha_{lm}\delta(t-T_l-\tau_{lm})\delta(\varphi-\Psi_l-\psi_{lm}) \tag{13}$$

where L, M_l, T_l, τ_{lm}, Ψ_l and ψ_{lm} denote the number of clusters, the number of rays in the l^{th} cluster, the arrival time of the l^{th} cluster, the arrival time of the m^{th} ray in the l^{th} cluster, the angle of arrival of the l^{th} cluster and that of the m^{th} ray in the l^{th} cluster, respectively. α_{lm} is a statistical complex-envelope gain of the m^{th} ray in the l^{th} cluster, where the amplitude follows a log-normal distribution, and the phase follows a uniform distribution [23].

3.2. MIMO Extension

To extend the TSV channel model to support MIMO scenarios, a geometrical approach is considered, as shown in Fig. 3. It can be noted that for a transmission in mmWave band, the effect of the distance between different Tx and Rx antennas is significant. For simplicity, we consider the uniform linear antenna arrays, where the Tx and Rx antennas are distributed vertically.

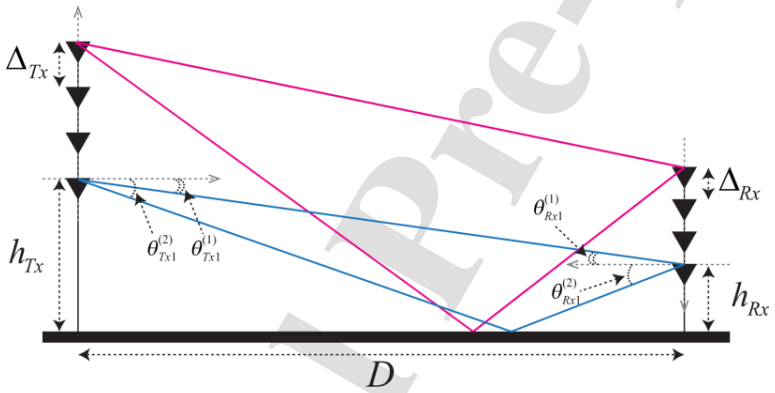

Fig. 3. MIMO extension of the TSV channel Model.

For $N_R \times N_T$ MIMO systems, the received signal Y is described by

$$Y=\boldsymbol{H}\,X+n \tag{14}$$

where X, n, N_T and N_R are the transmitted signal, the additive channel noise, the number of transmit antennas and the number of receive antennas, respectively. $\boldsymbol{H}$ is the $N_R \times N_T$ channel matrix represented by

$$\boldsymbol{H}=\begin{pmatrix} h_{1,1} & h_{1,2} & \cdots & h_{1,N_T} \\ h_{2,1} & h_{2,2} & \cdots & h_{2,N_T} \\ \vdots & \vdots & \ddots & \vdots \\ h_{N_R,1} & h_{N_R,2} & \cdots & h_{N_R,N_T} \end{pmatrix} \tag{15}$$

Each element $h_{i,k}(i \le N_R$ and $k \le N_T)$ of the matrix $\boldsymbol{H}$ can be expressed according to the TSV channel model. For LoS components, the gain $\beta_{i,k}$ between the k^{th} transmit antenna and the i^{th} receive antenna is given by

$$\beta_{i,k} = \left(\frac{\lambda}{4\pi D}\right)^2 \left| \sqrt{G_{Tx}^{(1)} G_{Rx}^{(1)}} \exp\left[-j\frac{2\pi\,(d_{i,k}^{(1)} - d_{1,1}^{(1)})}{\lambda}\right] + \sqrt{G_{Tx}^{(2)} G_{Rx}^{(2)}} R_0 \exp\left[j\frac{2\pi}{\lambda}\frac{2h_{Tx}h_{Rx}}{D}\right] \exp\left[-j\frac{2\pi\,(d_{i,k}^{(2)} - d_{1,1}^{(2)})}{\lambda}\right] \right| \quad (16)$$

where for p = 1,2,

$$\left[d_{i,k}^{(p)}\right]^2 = \left[d_{1,1}^{(p)} - (i-1)\Delta_{Rx}\, sin\,\theta_{Rx1}^{(p)} + (k-1)\Delta_{Tx}\, sin\,\theta_{Tx1}^{(p)}\right]^2 + \left[(k-1)\Delta_{Tx}\, cos\,\theta_{Tx1}^{(p)} + (i-1)\Delta_{Rx}\, cos\,\theta_{Rx1}^{(p)}\right]^2 \quad (17)$$

where $d_{i,k}^{(p)}$ is the distance between the k^{th} transmit antenna and the i^{th} receive antenna along path p. $\Delta_{Tx}, \Delta_{Rx}, \theta_{Tx1}^{(p)}$ and $\theta_{Rx1}^{(p)}$ are the Tx antenna separation, the Rx antenna separation, the angle of departure (AoD) of the path p and the angle of arrival (AoA) of the path p, respectively. For the NLoS path components, each element of matrix $\boldsymbol{H}$ can be calculated using SV channel model in the same way as in a SISO scenario.

4. Results and discussion

A global simulation of our proposed system is carried out using MATLAB/OptiSystem co-simulation platform proposed and used in our previous works [20,21]. The electrical up-conversion and the optical link are implemented in OptiSystem, while all other processes are performed using MATLAB. Data bits are generated and encoded according to the 5G NR specifications for multiplexing and channel coding [24]. The encoding processing includes cyclic redundancy check (CRC) attachment, code block segmentation, LDPC coding and rate matching. The encoded bits are mapped using QPSK, 16-QAM, and 64-QAM. The complex symbols are fed to the OFDM modulator to generate four baseband MIMO signals. Channel estimation pilots and Cyclic Prefix (CP) are added to the signals, then a Digital-to-Analogue Conversion (DAC) is performed. We have used the parameters defined in Table 2 to generate the OFDM MIMO signal, which occupies the 7,2 GHz bandwidth.

Table 2. Parameters used to generate OFDM MIMO signal.

Parameter	Value
Sampling rate	10 GS/s
FFT/IFFT size	512
Number of used data subcarriers	336
Number of pilot subcarriers	32
Cyclic Prefix	64

The resulting signals fed our optical architecture specified above. The main parameters of this architecture used for simulation are shown in Table 3. The 60 GHz signals at the output of PDs are transmitted over the 4x4 MIMO channel. To achieve this, a channel matrix is generated according to the 4x4 MIMO extension of the TSV model. At the receiver, the inverse processes are done. Channel estimation at pilot positions with arithmetic averaging is implemented according to the Least Squares (LS) criterion. The obtained channel coefficients are then interpolated to obtain the estimated channel coefficients at data positions. To reduce MIMO channel effects, Zero-Forcing Successive Interference Cancellation (ZF-SIC) detector is implemented.

Table 3. Main parameters of the optical architecture simulation.

Parameter	Value

Optical wavelength	1550 nm
Optical frequency	193.41 THz
Transmit power	0-16 dBm
Fiber length	5 km, 25 km, 50 km and 75 km
Fiber attenuation	0.2 dB/km
Dispersion	16.75 (ps/nm)/km
DD-MZM switching voltage	8 volt

Firstly, we have configured the optical architecture without Additive White Gaussian Noise (AWGN) and without the TSV MIMO channel. The choice of the transmit laser power P_{Laser} has been found by simulation as illustrated in Fig. 4, where the Error Vector Magnitude (EVM) of the received 16-QAM OFDM signals is calculated for 25 km of optical fiber length for different values of transmitting laser power injected in the optical modulators. We can see that a value of $P_{Laser} = 7$ dBm offers the best performance in terms of reducing the degradation caused by the nonlinearity of the optical component and optical fiber.

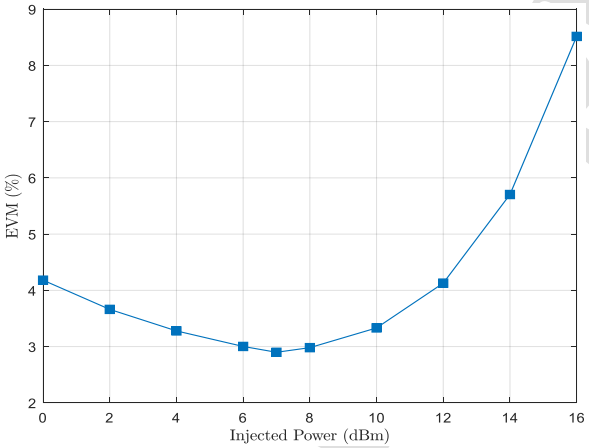

Fig. 4. Effect of the transmit laser power on the EVM of 16-QAM OFDM signals for 25 km of optical fiber length.

Fig. 5 (a) shows the power spectrum of the optical MIMO signals modulated using the DP-MZM. As we can see, the four signals are well placed at frequencies $f_c - f_{LO2}$, $f_c - f_{LO1}$, $f_c + f_{LO1}$, and $f_c + f_{LO2}$. Fig. 5 (b) shows the optical subcarriers, that correspond to the 1^{st} and 2^{nd} sidebands, generated by the DD-MZM. As shown, the optical carrier of frequency $f_c = 193.41$ THz is suppressed. The power spectrum of the combined signals to be transmitted over the optical fiber is shown in Fig. 5 (c). It can be seen that the spacing of 60 GHz is guaranteed between each data-signal spectrum and its corresponding subcarrier.

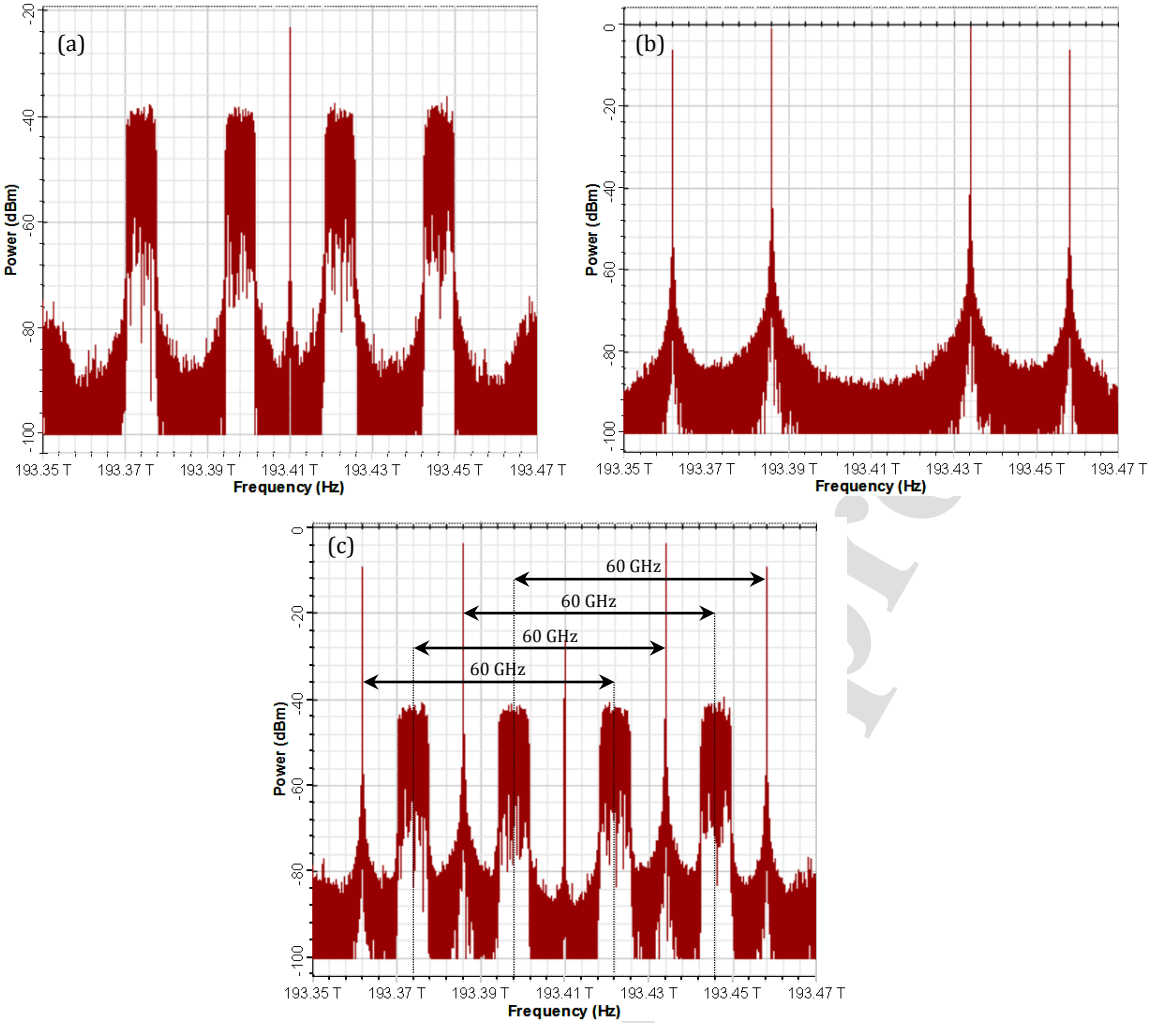

Fig. 5. (a) The optical spectrum of data-signals generated by DP-MZM, (b) The optical subcarriers generated by the DD-MZM, (c) The combined signals to be transmitted over fiber.

We have demonstrated in Fig. 6, the effect of the optical fiber length on the EVM performance of the optical link, using only the AWGN channel for different values of energy per bit to noise power spectral density ratio (Eb/No). The obtained values are compared with the EVM threshold of 12.5% defined by 3GPP requirements for 16-QAM modulation [28]. This required level is achieved for an optical fiber with a length ranging from 5 to 25 km and an Eb/No ratio of 5 dB.

In order to add the effect of the MIMO radio channel, we have generated the channel matrix for different Δ_{Tx} and Δ_{Rx} antenna separations. Then, we evaluated the performance of the 16-QAM 4x4 MIMO system, in terms of EVM versus antenna separation, without using the optical link, as shown in Fig. 7. As we can see, EVM performance changes quickly by changing antenna separation. This variation is due to the significant phase rotation created by the difference in distance between the two signal paths at 60 GHz. To guarantee sufficient field decorrelation in MIMO antennas, we have chosen the antennas separation of $\Delta_{Tx} = 8$ mm and $\Delta_{Rx} = 8$ mm, which correspond here to the minimum value of EVM. The chosen value of the antennas separation of 8 mm represents 1,6 times the wavelength of the RF carrier at 60 GHz.

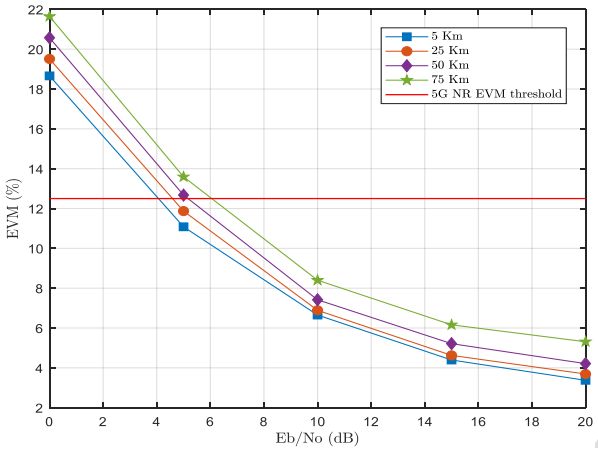

Fig. 6. Effect of the optical length on the EVM of the system using only the AWGN channel.

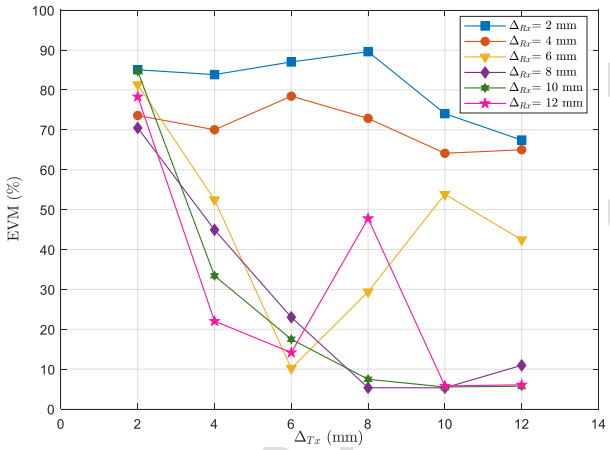

Fig. 7. EVM performance for different MIMO antenna separations.

To show the effect of radio channel length on performance, we have calculated the EVM in function of the channel length, as shown in Fig. 8. A strong degradation is noticed from the length of 6 m. This degradation is due to high level of attenuation present in the desktop environment of TSV channel at 60 GHz. In the rest of this paper, we have chosen to use the radio channel with length of 3 m. This distance corresponds to the average size of a small office room. Also, it is considered in several works and validated by experimental results as indicated in reference [23].

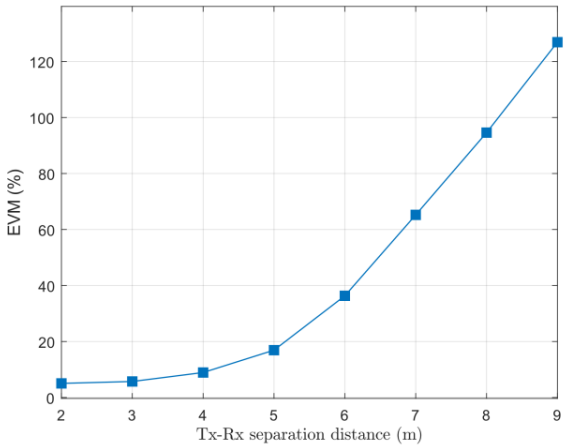

Fig. 8. EVM in function of radio channel length at Eb/No of 20 dB.

Next, we have evaluated the performance of our global RoF system that includes both the effect of the optical fiber of 25 km and the radio MIMO channel. Fig. 9 shows the obtained BER as a function of Eb/No for QPSK with data rate of 46,64 Gb/s, 16-QAM with data rate of 93,28 Gb/s and 64-QAM with data rate of 140 Gb/s, without using 5G NR channel coding. As we can see, a BER of 10^{-3} can be achieved by QPSK, and 16-QAM at Eb/No of 17 dB and 22 dB, respectively.

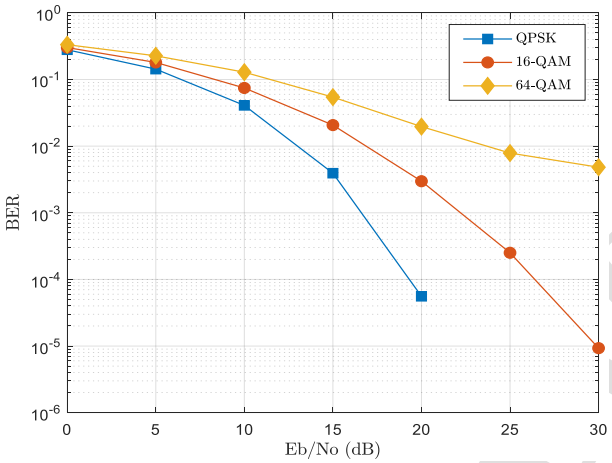

Fig. 9. BER performance of the global RoF system using uncoded QPSK, 16-QAM and 64-QAM.

To improve the quality of transmission and to meet 5G NR specifications, we have implemented the channel coding blocks. Fig. 10 presents the BER performance of 64-QAM using CRC, LDPC and rate matching for different coding rates. As shown, a significant improvement in terms of BER is achieved comparing with the uncoded 64-QAM. A BER of 10^{-6} can be reached with Eb/No of 10 dB using coding rate of 1/2. In addition, using these coding blocks can improve the data rate of the global system. Indeed, the data rate of transmitting 64-QAM signal with coding rate of 1/2 which corresponds to 70 Gb/s, exceeds the data rate of the uncoded QPSK signal with a BER performance enhancement. The same observation is noted, compared to uncoded 16-QAM, for 64-QAM with coding rates of 3/4 and 7/8, which correspond to data rates of 105 Gb/s and 122.5 Gb/s, respectively.

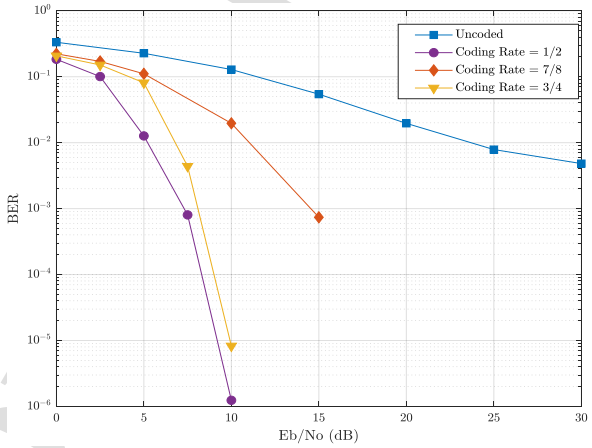

Fig. 10. BER performance of 64-QAM using 5G NR channel coding blocks for different rates.

5. Conclusion

In this paper, we presented a new 4x4 MIMO RoF architecture for 5G indoor mmWave applications. The proposal allows the transmission of 60 GHz OFDM MIMO signal over the optical fiber and performs heterodyne detection at the RAP level to reduce its cost and complexity. The optical architecture is based on DP-MZM for data optical modulation and DD-

MZM for optical subcarrier generation by exploiting its optical sidebands. To evaluate this scheme under a realistic indoor scenario, we have proposed a 4x4 MIMO extension of the well-known TSV channel model. For performance evaluation purposes, we have configured the optical power injected in the optical modulators and the MIMO antennas separation based on simulation results. The global RoF system is investigated in terms of BER versus of Eb/No for uncoded QPSK, 16-QAM, and 64-QAM schemes. Good performance is observed for uncoded QPSK and 16-QAM. To meet 5G NR specifications, we have implemented the channel coding techniques proposed by 3GPP. Significant improvement in terms of BER of 64-QAM is achieved using different coding rates. Also, data rate enhancement up to 122.5 Gb/s can be noticed by comparing coded 64-QAM with uncoded QPSK and uncoded 16-QAM under enhanced BER performance.

References

[1] K. Husenovic, I. Bedi, S. Maddens, I. Bozsoki, D. Daryabwite, N. Sundberg, M. Maniewicz, ITU, Setting the scene for 5G: Opportunities & Challenges, 2018.

[2] 3GPP, Technical Specification Group Services and System Aspects, release 15, TR 21.915 Version 15.0.0. (2019).

[3] V.W.S. Wong, R. Schober, D.W.K. Ng, L. Wang, Key Technologies for 5G Wireless Systems, Cambridge University Press, 2017. https://doi.org/10.1017/9781316771655.

[4] Z. Gao, L. Dai, D. Mi, Z. Wang, M.A. Imran, M.Z. Shakir, MmWave massive-MIMO-based wireless backhaul for the 5G ultra-dense network, IEEE Wirel. Commun. 22 (2015) 13–21. https://doi.org/10.1109/MWC.2015.7306533.

[5] J. Kim, M. Sung, S.H. Cho, Y.J. Won, B.C. Lim, S.Y. Pyun, J.K. Lee, J.H. Lee, MIMO-Supporting Radio-Over-Fiber System and its Application in mmWave-Based Indoor 5G Mobile Network, J. Light. Technol. 38 (2020) 101–111. https://doi.org/10.1109/JLT.2019.2931318.

[6] 3GPP, Technical Specification Group Services and System Aspects, release 17, TR 21.917 Version 1.0.0. (2022).

[7] T. Baykas, C.-S. Sum, Z. Lan, J. Wang, M. Rahman, H. Harada, S. Kato, IEEE 802.15.3c: the first IEEE wireless standard for data rates over 1 Gb/s, IEEE Commun. Mag. 49 (2011) 114–121. https://doi.org/10.1109/MCOM.2011.5936164.

[8] E. Perahia, C. Cordeiro, M. Park, L.L. Yang, IEEE 802.11ad: Defining the Next Generation Multi-Gbps Wi-Fi, in: 2010 7th IEEE Consum. Commun. Netw. Conf., IEEE, 2010: pp. 1–5. https://doi.org/10.1109/CCNC.2010.5421713.

[9] Y. Ghasempour, C.R.C.M. da Silva, C. Cordeiro, E.W. Knightly, IEEE 802.11ay: Next-Generation 60 GHz Communication for 100 Gb/s Wi-Fi, IEEE Commun. Mag. 55 (2017) 186–192. https://doi.org/10.1109/MCOM.2017.1700393.

[10] S. Lagen, L. Giupponi, S. Goyal, N. Patriciello, B. Bojovic, A. Demir, M. Beluri, New Radio Beam-Based Access to Unlicensed Spectrum: Design Challenges and Solutions, IEEE Commun. Surv. Tutorials. 22 (2020) 8–37. https://doi.org/10.1109/COMST.2019.2949145.

[11] M. Hirzallah, M. Krunz, B. Kecicioglu, B. Hamzeh, 5G New Radio Unlicensed: Challenges and Evaluation, IEEE Trans. Cogn. Commun. Netw. 7 (2021) 689–701. https://doi.org/10.1109/TCCN.2020.3041851.

[12] A. Daraseliya, M. Korshykov, E. Sopin, D. Moltchanov, S. Andreev, K. Samouylov,

Coexistence analysis of 5g nr unlicensed and wigig in millimeter-wave spectrum, IEEE Trans. Veh. Technol. 70 (2021) 11721–11735. https://doi.org/10.1109/TVT.2021.3113617.

[13] X. Lu, V. Petrov, D. Moltchanov, S. Andreev, T. Mahmoodi, M. Dohler, 5G-U: Conceptualizing Integrated Utilization of Licensed and Unlicensed Spectrum for Future IoT, IEEE Commun. Mag. 57 (2019) 92–98. https://doi.org/10.1109/MCOM.2019.1800663.

[14] A.G. Armada, V.A. Thomas, M. El-Hajjar, L. Hanzo, Radio-over-Fiber Aided Base Station Coordination for OFDM, in: 2014 IEEE 80th Veh. Technol. Conf., IEEE, 2014: pp. 1–6. https://doi.org/10.1109/VTCFall.2014.6966148.

[15] J. Beas, G. Castanon, I. Aldaya, A. Aragon-Zavala, G. Campuzano, Millimeter-Wave Frequency Radio over Fiber Systems: A Survey, IEEE Commun. Surv. Tutorials. 15 (2013) 1593–1619. https://doi.org/10.1109/SURV.2013.013013.00135.

[16] N.M. Akshatha, P. Jha, A. Karandikar, A Centralized SDN Architecture for the 5G Cellular Network, in: 2018 IEEE 5G World Forum, IEEE, 2018: pp. 147–152. https://doi.org/10.1109/5GWF.2018.8516960.

[17] J. Capmany, B. Ortega, A. Martinez, D. Pastor, M. Popov, P.Y. Fonjallaz, Multiwavelength single sideband modulation for WDM radio-over-fiber systems using a fiber grating array tandem device, IEEE Photonics Technol. Lett. 17 (2005) 471–473. https://doi.org/10.1109/LPT.2004.840017.

[18] H. Huang, C. Sun, C. Lin, C. Wei, W. Zeng, H. Chang, B. Shih, A. Ng'oma, Direct-Detection PDM-OFDM RoF System for 60-GHz 2×2 MIMO Wireless Transmission Without Polarization Tracking, J. Light. Technol. 36 (2018) 3739–3745. https://doi.org/10.1109/JLT.2018.2840102.

[19] C.-H.C.-T. Lin, C.-H.C.-T. Lin, H.-T. Huang, W.-S. Zeng, S.-C. Chiang, H.-Y. Chang, 60-GHz optical/wireless MIMO system integrated with optical subcarrier multiplexing and 2x2 wireless communication, Opt. Express. 23 (2015) 12111. https://doi.org/10.1364/oe.23.012111.

[20] M. El Yahyaoui, A. El Moussati, G. El Zein, On the capacity of MIMO-OFDM based diversity and spatial multiplexing in Radio-over-Fiber system, Opt. Commun. 402 (2017) 252–259. https://doi.org/10.1016/j.optcom.2017.05.078.

[21] M. El Yahyaoui, A. El Moussati, G. El Zein, K. Haddadi, New millimeter wave generation scheme for MIMO-OFDM based Radio-over-Fiber system, Opt. Commun. 442 (2019) 101–105. https://doi.org/10.1016/j.optcom.2019.03.017.

[22] W.J. Witteman, Detection and Signal Processing, Springer Berlin Heidelberg, Berlin, Heidelberg, 2006. https://doi.org/10.1007/978-3-540-29600-3.

[23] Y. Shoji, H. Sawada, Chang-Soon Choi, H. Ogawa, A Modified SV-Model Suitable for Line-of-Sight Desktop Usage of Millimeter-Wave WPAN Systems, IEEE Trans. Antennas Propag. 57 (2009) 2940–2948. https://doi.org/10.1109/TAP.2009.2029286.

[24] 3GPP, 5G ; NR; Multiplexing and channel coding Release 16, TS 38.212 Version 16.2.0. (2020).

[25] H. Yang, S. Zheng, S. Xu, J. Ji, F. Li, X. Zhang, A general analytical method for suppressing the third-order intermodulation in microwave photonic link based on dual-parallel Mach–Zehnder modulator, Opt. Commun. 458 (2020) 124818. https://doi.org/10.1016/j.optcom.2019.124818.

[26] F. Ujang, T. Firmansyah, P.S. Priambodo, G. Wibisono, Irregular Shifting of RF Driving Signal Phase to Overcome Dispersion Power Fading, Photonics. 6 (2019) 104. https://doi.org/10.3390/photonics6040104.

[27] Hirokazu Sawada, Yozo Shoji, Chang-Soon Choi, Proposal of novel statistic channel model for millimeter wave WPAN, in: 2006 Asia-Pacific Microw. Conf., IEEE, 2006: pp. 1855–1858. https://doi.org/10.1109/APMC.2006.4429770.

[28] 3GPP, 5G; NR; User Equipment (UE) radio transmission and reception; Part 1: Range 1 Standalone, release 15, TS 38.101-1 Version 15.3.0. (2018).

1. New 4x4 MIMO RoF scheme is proposed to transmit 5G mmWave signals.

2. MIMO extension of the TSV radio channel model is introduced and used.

3. Performance evaluation of the proposed RoF system with and without 5G NR channel coding.

Declaration of interests

☒ The authors declare that they have no known competing financial interests or personal relationships that could have appeared to influence the work reported in this paper.

☐ The authors declare the following financial interests/personal relationships which may be considered as potential competing interests: